Author's personal copy

Polymer 53 (2012) 3928–3936

Contents lists available at SciVerse ScienceDirect

Polymer

journal homepage: www.elsevier.com/locate/polymer

Effects of mesomorphic β nanograins on crystallization and photoexcited emission of poly(9,9-di-*n*-hexyl-2,7-fluorene)

Wei-Ru Wu [a,b], Wei-Tsung Chuang [a], U-Ser Jeng [a,b,*], Chun-Jen Su [a], Su-Hua Chen [c], Chun-Yu Chen [a], Chiu-Hun Su [a,d], An-Chung Su [b,**]

[a] National Synchrotron Radiation Research Center, Hsinchu Science Park, Hsinchu 30076, Taiwan
[b] Department of Chemical Engineering, National Tsing Hua University, Hsinchu 30013, Taiwan
[c] Department of Materials Science and Engineering, National Dong Hwa University, Hualien 97401, Taiwan
[d] Industrial Technology Research Institute, Hsinchu 31040, Taiwan

ARTICLE INFO

Article history:
Received 2 April 2012
Received in revised form
24 June 2012
Accepted 12 July 2012
Available online 20 July 2012

Keywords:
Mesomorphic nanograins
Polyfluorenes
SAXS/WAXS/DSC

ABSTRACT

Structural evolution processes of solution-cast and melt-quenched poly(9,9-di-*n*-hexyl- 2,7-fluorene) (PFH) were quantitatively examined using small/wide-angle X-ray scattering (SAXS/WAXS) and differential scanning calorimetry. SAXS/WAXS profiles of solution-cast PFH indicated presence of nanograins (radius of gyration $R_g \approx 5$ nm) of 2D-ordered β phase. Upon heating above T_g, perfected packing order and growth of β nanograins up to $R_g \approx 10$ nm result in suppressed formation of α crystallites up to 190 °C, beyond which extensive melting accompanied by significant (albeit partial) transformation of β nanograins into α nanocrystals of $R_g \approx 13$ nm can be observed in a narrow temperature range of 190–200 °C. Thus transformed α crystallites remained stable in size before melting above 235 °C. The nanograin structures observed are correlated to phase-dependent optical absorption and photoexcited emission. Results suggest sensitive influences of the size/spatial distribution of β nanograins (particularly in the layering direction of the 2D-ordered chain packing) on photoexcited emission of the polyfluorene film.

© 2012 Elsevier Ltd. All rights reserved.

1. Introduction

Owing to their variegated phase behavior and potential application in the polymer light emitting diode, polyfluorenes have been extensively studied in recent years [1–5]. Comprehending the relationship of fundamental property and phase behavior of polyfluorene may significantly ameliorate the development of conducting polymers for electroluminescence devices. Particularly, the β phase of polyfluorenes, having more extended conjugation than the glassy phase, was shown to have profound influences on blue emission and hole mobility [2–5]. Although the electronic structures [2–5] and gelation behavior [6] of the β-phase of polyfluorenes have been extensively studied, morphological details in mesoscale and the related structural evolution of the mesomorphic β phase in the solution-cast films prior to crystallization are much less explored. As the rich phase morphology of polyfluorenes provides a unique opportunity to manipulate the photoemission and hole transport properties without the need of chemical modification, detailed structural features of β phase may provide useful implications in film processing for tuning electroluminescence behavior of polyfluorene-based light emitting diodes.

Moreover, the rich phase formations and transitions carrying in the polyfluorene-based polymer films also provide a good platform for studying the characteristics of chain preordering in mesomorphic phases as well as the related evolution into a final crystalline form [1,7,8]. Recently, increasingly more experimental evidences from microscopic techniques have demonstrated that polymer crystal surfaces often comprise nodules in the nanometer-sized scale [1,7,8]. Complementary to imaging studies, X-ray and light scattering observations in a number of polymeric materials suggest a precursory ordering process prior to crystallization [9–21]. By means of in situ small-/wide-angle X-ray scattering (SAXS/WAXS) and differential scanning calorimetry (DSC), structural evolution during cold crystallization of poly(9,9-di-*n*-octyl-2,7-fluorene) (PFO) [19], syndiotactic polystyrene (sPS) [20], and poly(trimethylene terephthalate) (PTT) [21], were quantitatively examined. Simultaneous SAXS/WAXS profiles obtained upon programmed

* Corresponding author. National Synchrotron Radiation Research Center, 101 Hsin-Ann Road, Hsinchu Science Park, Hsinchu 30076, Taiwan. Tel.: +886 3 578 0281; fax: +886 3 578 3813.
** Corresponding author. 101, Section 2, Kuang-Fu Road, Hsinchu 30013, Taiwan. Tel.: +886 3 5715131 33683; fax: +886 3 5715408.
E-mail addresses: usjeng@nsrrc.org.tw (U.-S. Jeng), acsu@mx.nthu.edu.tw (A.-C. Su).

0032-3861/$ – see front matter © 2012 Elsevier Ltd. All rights reserved.
http://dx.doi.org/10.1016/j.polymer.2012.07.024

Author's personal copy

heating unveiled a common sequence of stages toward crystallization, including (1) a frozen-in stage below the glass transition temperature T_g, (2) the nucleation of precursory nanograins with a constant size of several nanometers right above T_g, (3) growth of the nanograins with crystallization taking place inside, and (4) coalescence/thickening of crystalline nanograins up to a temperature-dependent size upon contact of nanograins.

In previous studies, four different phases for poly(9,9-di-*n*-hexyl-2,7-fluorene) (PFH) were identified [1,22] via WAXS, DSC, and electron microcopy. The WAXS profile of the as-cast film revealed a mesomorphic β phase with layer spacing of ca. 1.4 nm. This β phase (as a degenerate structure after evaporation of the caged solvent molecules) [23,24], is metastable and transforms into the crystalline α form when heated above 175 °C. The α crystallites melt into a nematic (*N*) liquid when heated above 250 °C. Subsequently, upon stepwise cooling, the nematic melt crystallizes into α phase first, followed by solid–solid transformation into another crystalline (α′) form. The determined crystalline structure of α form is monoclinic (with unit cell parameters $a = 2.15$ nm, $b = 2.47$ nm, $c = 3.32$ nm, and $\beta = 96°$) whereas that of α′ form is triclinic (with cell parameters $a = 2.05$ nm, $b = 2.58$ nm, $c = 3.30$ nm, $\alpha = 84°$, $\beta = 96°$, and $\gamma = 90°$). The nomenclature of these PFH phases actually originated from similar phases in its most extensively studied homolog, poly(9,9-di-*n*-octyl-2,7-fluorene) (PFO) [8,25,26]. In both cases, the β phase serves as an intermediate stage of transformation midway from a solvent-induced structure toward the crystalline phase. The β phase of PFH, however, is higher-melting (ca. 185 vs. 105 °C) and better ordered [1,22], ideal for the study of transformation of mesomorphic nanodomains into 3D crystalline order for comparison with previous cases of nematic-like precursors [19–21,27]. Previously, characteristically different couplings of crystallization behavior with respect to smectic vs. isotropic surroundings were revealed via a polyester composed of heptamethylene-bibenzoate units and heptamethylene-terephthalate co-units [28].

The main objective of the present work is to elucidate via SAXS/WAXS/DSC the mesophase (β vs. nematic) modulated crystallization behavior of PFH and the structural development process during the β-to-α transformation in the solvent-cast PFH film. The structural characteristics observed are correlated to the phase-dependent optical absorption and photoexcited emissions measured to give implications that may be helpful in tailoring the film morphological features for specific optical properties.

2. Experimental details

2.1. Materials and specimen preparation

Purchased from American Dye Source, Quebec, the PFH material was ca. 45 kDa in weight-average molecular mass (M_w) and ca. 2.8 in polydispersity, as determined from size exclusion chromatography with polystyrene standards. Glassy PFH specimens (ca. 0.5 mm in thickness and 6 mm in diameter) were ice-water quenched from the nematic phase at 280 °C whereas β-rich thin films were drop-cast on glass substrates from 1 w/v% toluene solution, detached, cut, stacked and compressed into disks 0.5–1.0 mm in thickness and ca. 6 mm in diameter at 0.5 Mbar. These were placed in standard aluminum cells for DSC, with the cap and the pan punctured and then sealed by 8-μm Kapton films to give X-ray windows of 4 mm in diameter.

2.2. SAXS/WAXS/DSC during programmed heating

Simultaneous SAXS/WAXS/DSC was performed at the SWAXS endstation of the 23A wiggler beamline of the National Synchrotron Radiation Research Center (NSRRC), Hisnchu [29]. With the encapsulated specimen placed in the modified Mettler Toledo FP84 DSC cell holder (detailed previously) [19], SAXS, WAXS, and DSC data were simultaneously collected using a Mar CCD165 area detector (165 mm in diameter) for SAXS and a linear-proportional gas detector for WAXS during programmed heating from 30 to 280 °C at 10 °C/min. Limited by the geometrical constraints of the simultaneous SAXS/WAXS/DSC instrument used [29], a beam of low X-ray energy of 6 keV (2.07 Å) was needed to cover simultaneously the scattering wavevector $q = 0.45$ Å in WAXS for the first critical reflection and $q \sim 0.004$ Å in SAXS for large spacing and a reliable subtraction of the scattering from a nematic matrix; together with the sample-to-detector distances 2200 and 1000 mm respectively for SAXS and WAXS, synchronized SAXS/WAXS data were collected with 1 frame per 15 s.

All SAXS data were rigorously corrected for electronic noise, sample transmission, background scattering and detector sensitivity, followed by calibration with polyethylene for absolute scattering intensity and silver behenate for the scattering wavevector $q \equiv 4\pi\lambda^{-1}\sin\theta_B$ in which the scattering angle is $2\theta_B$; the absolute intensity $I(q)$ (in units of cm^{-1}) is defined as differential cross-section per unit volume of a sample [29]. The WAXS data, corrected for background scattering and detector sensitivity, were placed on the *q*-axis calibrated by the diffractions from sodalite powders [28]. Experimental reproducibility was generally confirmed by repeated runs using fresh specimens. In selected cases, the DSC experiment was repeated by use of a separate Perkin–Elmer Diamond instrument for better signal quality.

2.3. Temperature-resolved optical absorption and photoexcited emission spectroscopy

Optical absorption (UV–vis) and photoexcited emission (PL) spectra of the film specimens were obtained by use of a Labguide MFS-230 instrument of fiber optics design where the sample holder was modified to accommodate an ice water-cooled high temperature stage (Linkman THMS600, connected to a TMS-91 temperature controller) with quartz windows. Temperature was programmed to increase from room temperature to 280 °C at a rate of 10 °C/min. For PL measurements, a fixed excitation wavelength $\lambda_{exc} = 380$ nm was consistently adopted.

2.4. Data analysis

SAXS data analysis follows closely that reported previously [19–21]. Briefly, the SAXS profiles were modeled by $I(q) = I_o P(q) S(q)$ with zero-angle scattering intensity I_o, form factor $P(q)$, and structure factor $S(q)$ [30,31]. An ellipsoid form factor with semi-major axis *A* and semi-minor axis *B* together with and a structure factor $S(q)$ based on Percus–Yevick model [30,31] with hard sphere potential were used in the SAXS data fitting to obtain the nanograin size, shape, and interparticle distance *d*. The scattering invariant $Q_{inv} = \int I(q)\, q^2\, dq$ within the experimental *q*-range was used to quantify the level of heterogeneity in the approximated two-phase system (nanograins in the amorphous matrix) [19–21]. The *relative* crystallinity $X_{c,WAXS}$, obtained from the WAXS profile based on the integrated intensity over the observed crystalline reflections, was normalized with respect to the *maximum* crystallinity observed; the final melting profile of the same sample was used as an amorphous reference. Likewise, the relative crystallinity $X_{c,DSC}$, obtained from a DSC trace based on the integrated heat flow up to temperature *T*, was normalized to the *total* heat flow integrated over the entire DSC trace.

Author's personal copy

3. Results and discussion

3.1. Cold-crystallization in the presence of β phase

Temperature-dependent SAXS profiles of the as-cast β-rich PFH specimen (Fig. 1a), indicate substantial excess scattering other than that contributed by the glassy matrix, presumably from solvent-induced β nanograins. Above the glass transition temperature ($T_g \approx 100$ °C) of PFH, the excess scattering started to increase further. Removal of the constant scattering of the glassy state from the as-obtained SAXS profiles at 120–240 °C during programmed heating at 10 °C/min gives the scattering contribution directly related to the structural evolution of solvent-induced PFH nanograins, as detailed below.

3.1.1. Growth/coalescence of β nanograins

From 120 to 180 °C, SAXS profiles in Fig. 1b display successive shifts of the interference peak from $q_c = 0.0217$ to 0.0140 Å^{-1}, whereas the peak intensity increases strongly with temperature by more than ten folds (from 0.75 to 8.33 cm^{-1}). We attribute the growing intensity mainly to size increase, as revealed by the fitted $P(q)$ and $S(q)$ profiles extracted. Using the ellipsoidal form factor and hard-sphere structure factor, we fitted respectively SAXS profiles at 120–180 °C (Fig. 1b) to obtain ellipsoid dimensions (A, B) = (3.4 nm, 7.5 nm)–(7.1 nm, 13.6 nm), with R_g increasing from 5.0 to 9.2 nm and d from 29 to 38 nm. To reconcile simultaneous increases in both the nanograin size and the inter-grain distance, as that similarly observed in previous studies [19,20], coalescence of nanograins is proposed in view of proximity between mean inter-grain spacing d and the long dimension ($2B$) of the ellipsoidal nanograins. Values of fitted parameters are summarized in Fig. 2. Note that fitting SAXS profiles at 120 and 130 °C with either Kratky–Porod approximation [31] (disc form) or the ellipsoid model gave comparable parametric values (cf. Fig. S1, Supporting information, SI), consistently indicating that the pre-existing β nanograins are oblate in shape ($A/B \approx 0.5$) in contrast to the prolate nuclei ($A/B \approx 2$) emerged from a nematic phase (detailed below). We have also tried $P(q)$ for spheres, rods, and disks in the SAXS data fitting; the ellipsoidal shape gives the best result. Moreover, the fitted dimensions $2A$ and $2B$ of the ellipsoidal nanograins are comparable with that given by the crystal sizes extracted from the WAXS data, as shown below.

Concomitant with the increase in nanograin size revealed via SAXS, gradual sharpening of the characteristic reflection at $q = 0.456$ Å^{-1} of the β phase is observed in this temperature range (cf. WAXS profiles in Fig. 1c), indicating general absence of α crystals [1,22]. The corresponding DSC trace (Fig. 1d) demonstrates a mild exotherm between 120 and 150 °C whereas there are no discernible

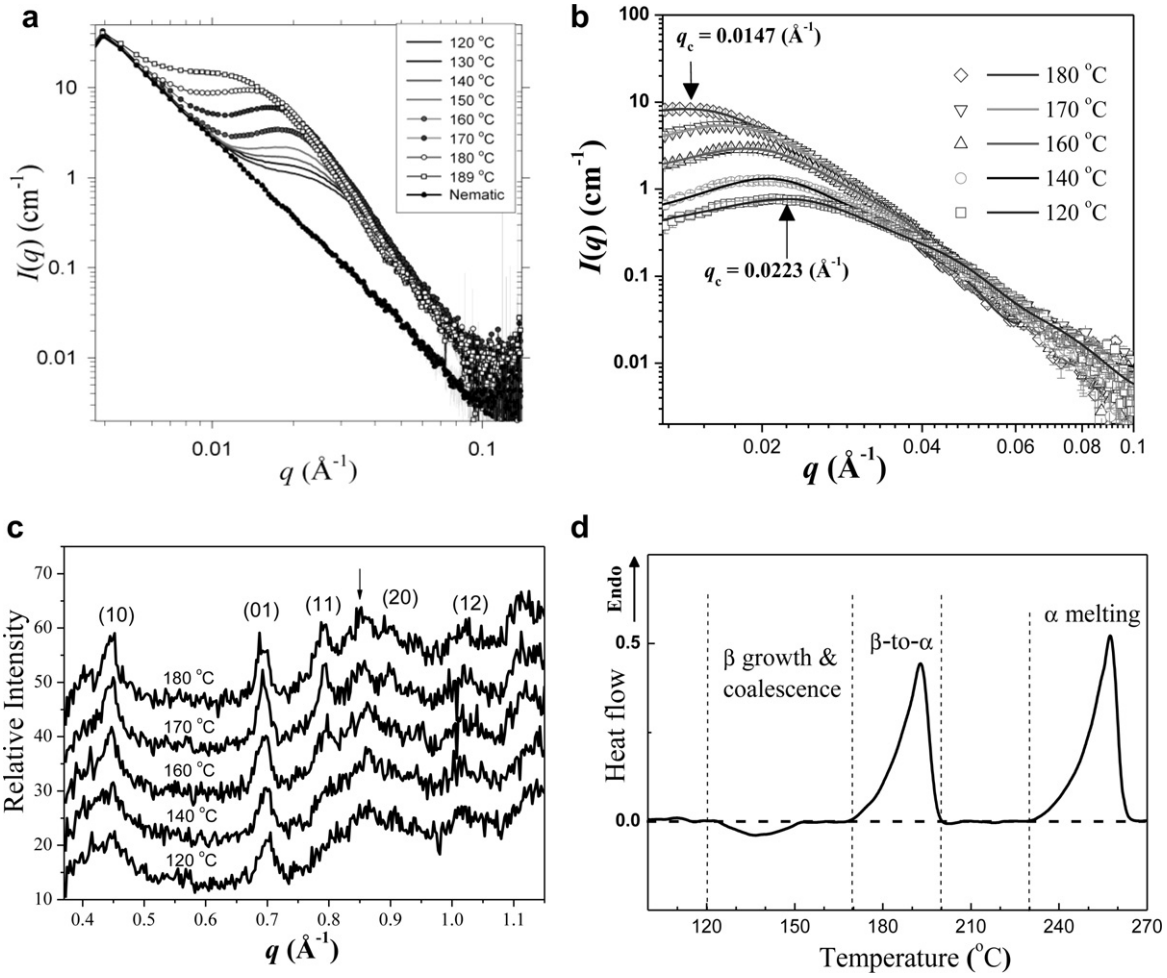

Fig. 1. (a) Representative temperature-dependent SAXS profiles obtained during heating of as-quenched PFH film from 120 to 189 °C. The profile of nematic melt at 270 °C is also given as reference. (b) SAXS profiles obtained at 120–180 °C for the solvent cast PFH film fitted using the ellipsoidal form factor and a hard-sphere structure factor $S(q)$. (c) Concurrently obtained WAXS profiles, with the gradually matured reflections of β phase indexed according to 2D square lattice parameters (a, b). The arrow indicates an unidentified peak at $q = 0.85$ Å^{-1}. (d) Corresponding DSC trace, with the characteristic temperatures marked by vertical lines.

Author's personal copy

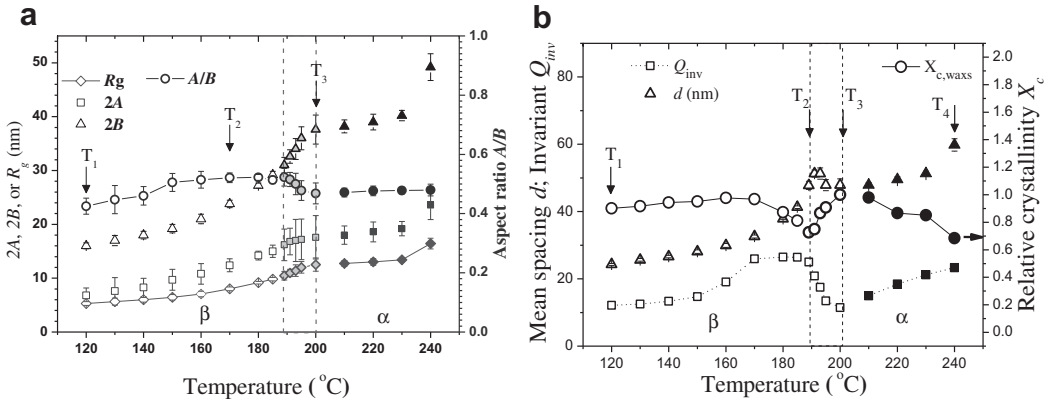

Fig. 2. (a) Changes in major axis 2*A* and minor axis 2*B*, aspect ratio *A*/*B*, and R_g of ellipsoidal nanograins during the programmed heating at 10 °C/min up to 240 °C for the solvent cast PFH film. (b) Changes in the fitted mean center-to-center intergrain spacing *d*, the normalized scattering invariant Q_{inv}, and normalized crystallinities extracted from the corresponding WAXS profiles ($X_{c,WAXS}$). Highlighted are onset temperatures of the growth and coalescence of β phase ($T_1 \approx 120$ °C), the starting ($T_2 \approx 190$ °C) and completing ($T_3 \approx 200$ °C) of the β-to-α transformation before final melting (240 °C) of α phase.

events in the following temperature range of 150–170 °C; these are indicative of growth and simultaneous coalescence before 150 °C and coalescence only afterward, in view of the clearly increased nanograin size, intergrain spacing, and increased crystallinity (cf. Fig. 2). Also observed is the concomitant crystal thickening, resulting in increased aspect ratio *A*/*B* from 0.42 to a plateau value of 0.52, characteristic to fully grown β nanograins (Fig. 2a). Consistent with the attribution of pure coalescence beyond 150 °C, a separate run of halted temperature rise at 160 °C results in little changes in SAXS and WAXS reflections beyond the first minute, indicating quick completion of the temperature-sensitive coalescence process.

In Fig. 1c, the gradually matured reflections of β phase can be indexed according to 2D square lattice parameters $(a, b) = (1.38\ \text{nm}, 0.88\ \text{nm})$. Previously, two similar *d*-spacings 1.22 nm and 0.87 nm were also observed for the β phase of PFO [1]. Very likely, *b* may correspond to the molecular structure of PFH with a monomer length of ca. 0.84 nm [1]. The larger characteristic length *a* may associate with a smectic-like layer spacing of the polyfluorene; as that similarly proposed for PFO with the 1.22 nm spacing [1]. This, however, would imply a different packing geometry of FPH from that for PFO, owing to the longer lamellar spacing with the shorter alkyl chain length. Correspondingly, in the case of PFH, the β-mesomorphic phase can develop much better and dissipate only after 189 °C, compared to ca. 100 °C of the PFO β phase [1]. Furthermore, an unidentified weak peak at $q = 0.85\ \text{Å}^{-1}$ (Fig. 1c) suggest underdeveloped order in the third dimension, that was not observable in the PFO case [1].

3.1.2. *Melting of β nanograins and emergence of α crystals*

Illustrated in Fig. 3a are SAXS profiles obtained at 189–200 °C with the contribution from the matrix subtracted. Successively decreased SAXS intensity and diminishing of the characteristic β reflections indicate melting of some β nanograins; corresponding WAXS profiles (Fig. 3b) demonstrate the quick disappearance of β phase between 190 and 195 °C and concomitant emergence of α crystalline peaks. There is a clear endotherm from 170 to 200 °C in the DSC trace (Fig. 1d), consistent with the notion of partial melting of β nanograins and the simultaneous formation of α nanograins in view of the lack of a crystallization exotherm. Despite α phase exists stably in the higher temperature region than β phase, the net endotherm, rather than exotherm, in the transition

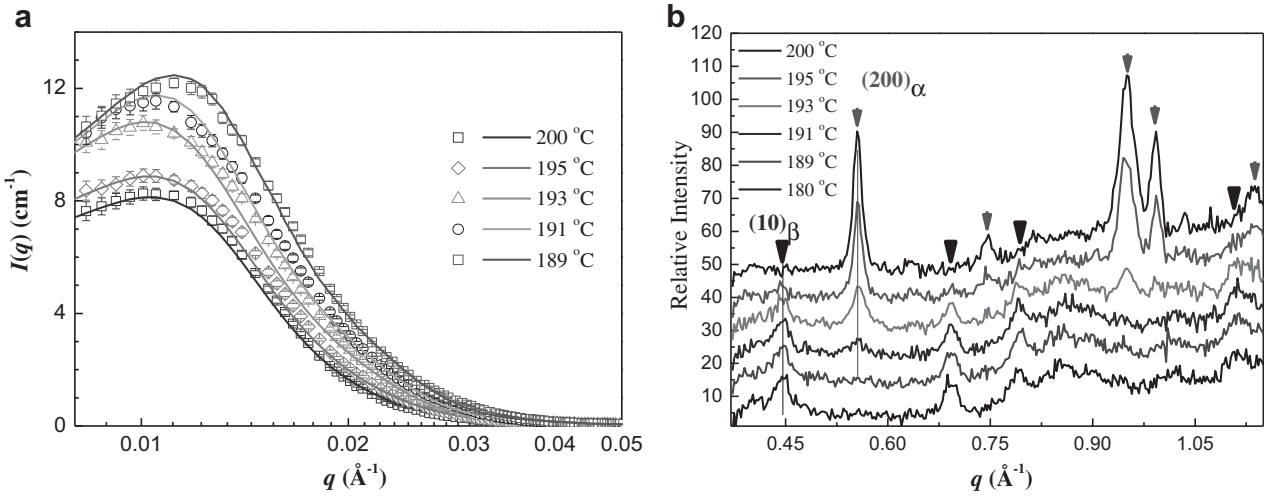

Fig. 3. (a) SAXS profiles obtained at 189–200 °C fitted using the ellipsoidal form factor and a hard-sphere structure factor $S(q)$, generally indicating partial melting of β nanograins. (b) Corresponding WAXS profiles demonstrating quick β (reflections marked by large arrows) to α (reflections marked by small arrows) transformation between 190 and 195 °C in the remaining nanograins.

Author's personal copy

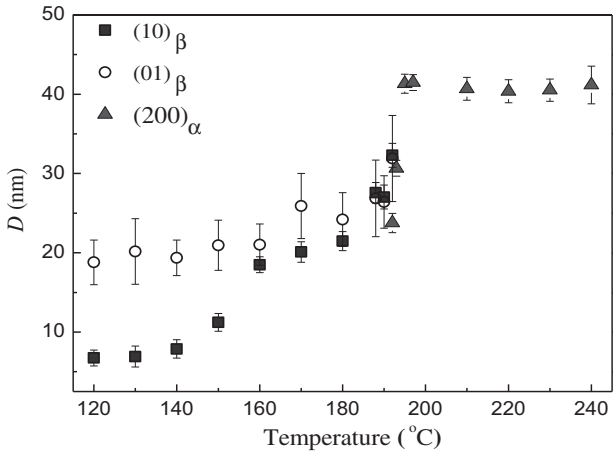

Fig. 4. Changes in lateral grain size with temperature as calculated from the Scherrer equation on the basis of (10) and (01) reflections of β phase or the $(200)_\alpha$ peak.

regime implies that melted β nanograins are significantly outnumbered that transforming into α nanograins. Complementarily, Q_{inv} indeed decreases upon the β-to-α transformation above 190 °C (Fig. 2b), supporting the non-quantitative conversion from β to α nanograins.

More quantitatively, the lateral size D of α and β nanodomains may be estimated from WAXS profile analysis for the full-width-half-maximum δq of the Bragg reflection of the $(200)_\alpha$ reflection and the (10) reflection of β, using the Scherrer equation $D = 2\pi K/\delta q$ (which is equivalent to the traditional form in terms of scattering angle) [32]. The shape factor $K = 0.95$ was used as an approximation, as α crystals of the polyfluorene system revealed spherulite features [8,32]. As shown in Fig. 4, this gives an estimate of a constant $D_\beta \approx 7$ nm for the as-cast film and that at 120 °C. Upon heating above T_g, D_β increases quickly with temperature (signifying growth of β nanograins, as supported by the concomitantly increasing $X_{c,WAXS}$ in Fig. 2b), reaching a plateau value of 25 nm above 160 °C before complete disappearance of β phase at 195 °C; in contrast, $D_{\beta(01)}$ grows relatively marginally from 18 nm to 25 nm. Interestingly, the newly formed α domain size is instantaneously large, with $D_\alpha \approx 25$–30 nm at 191–193 °C (comparable with D_β, implying in-situ transformation of pre-melted β into α nanograins), followed by sharp increase up to 42 nm at 195 °C (implying quick saturation through growth and possibly coalescence with neighboring β nanograins). The decrease of $X_{c,WAXS}$ from 170 to 190 °C and the subsequent increase of $X_{c,WAXS}$ from 190 to 200 °C (Fig. 2b) certainly correspond to disruption of β order and establishment of α packing, respectively; however, the nearly constant SAXS Q_{inv} (cf. Fig. 2b) indicates that the pre-melted β nanodomains were not yet dissipated (i.e., still of adequate density contrast) at 190 °C and hence could readily reorganize into α nanodomains. Nevertheless, Q_{inv} indeed decreases upon β-to-α transformation above 190 °C, indicating non-quantitative conversion from β to α nanograins. There were no hints for emergence of α nanograins from SAXS or WAXS profiles in the initial melting stage below 190 °C, consistent with the assumed absence of α nuclei in the nematic matrix. After transformation, SAXS and WAXS profiles showed no discernible changes from further annealing at 200 °C, demonstrating that the newly formed α phase indeed behaves similar to α nanograins in the coalescence stage of cold-crystallization, as delineated in Section 3.2.

3.1.3. Final melting

From 210 to 230 °C, SAXS profiles in Fig. 5a display a relatively stable interference peak position, which nevertheless shifts at 240 °C abruptly again from $q_c = 0.0118$ to 0.0087 Å^{-1}. We attribute this further growth in intensity at 240 °C mainly to size increase, as suggested by the fitted $P(q)$ and $S(q)$ profiles. Using the same ellipsoidal form factor and hard-sphere structure factor, we fitted respectively SAXS profiles at 210–240 °C to yield ellipsoid dimensions $(A, B) = (9.0\text{ nm}, 19.1\text{ nm})$ to $(11.8\text{ nm}, 24.6\text{ nm})$, with R_g increasing from 12.7 to 16.4 nm and d from 48 to 60 nm. Values of fitted parameters are summarized in Fig. 2. Concomitant with the increase in nanograin size revealed via SAXS, the WAXS profiles (Fig. 5b) demonstrate the steep decay of crystallinity $X_{c,WAXS}$ starting around 235 °C, which is before the active endothermic DSC signal at 240 °C (Fig. 2b), indicating more stringent definition of crystallinity by $X_{c,WAXS}$ in terms of lattice order as compared to thermal event. In this melting stage, the nanograin size, intergrain distance (cf. Fig. 2), and crystal size (cf. Fig. 4) remain stable until final melting starting at 235 °C, indicating relatively uniform size distribution in comparison with that from the nematic melt (detailed in Section 3.2); correspondingly, the parallel DSC trace (Fig. 1c) exhibits a single endotherm peak in the final melting.

The structural evolution of a solution-cast PFH film may be characterized by the stages of as-cast β nanograins, growth/coalescence of β nanograins, β-to-α transition, and pure crystalline α nanograins (cf. Fig. 6). Briefly, upon heating above T_g, perfection of order and growth of β nanograins (from a stable $R_g \approx 5$ nm up to

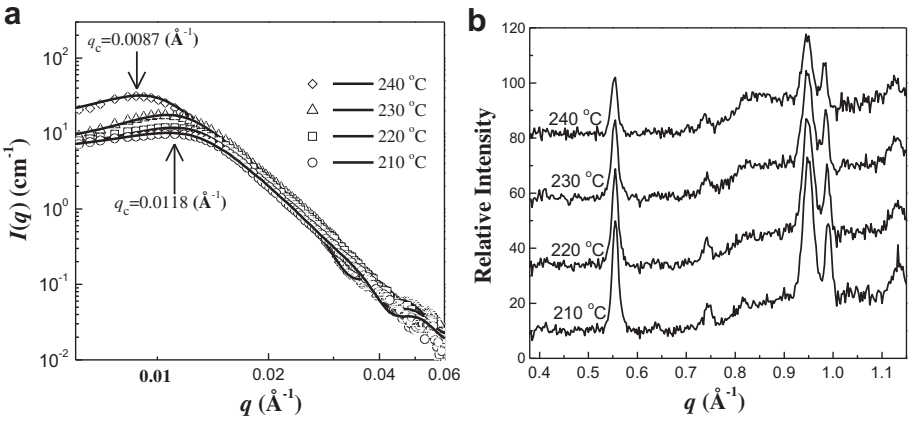

Fig. 5. (a) SAXS profiles obtained at 210–240 °C fitted using the ellipsoidal form factor and a hard-sphere structure factor $S(q)$. (b) Concomitant WAXS profiles during heating from 210 to 240 °C.

Author's personal copy

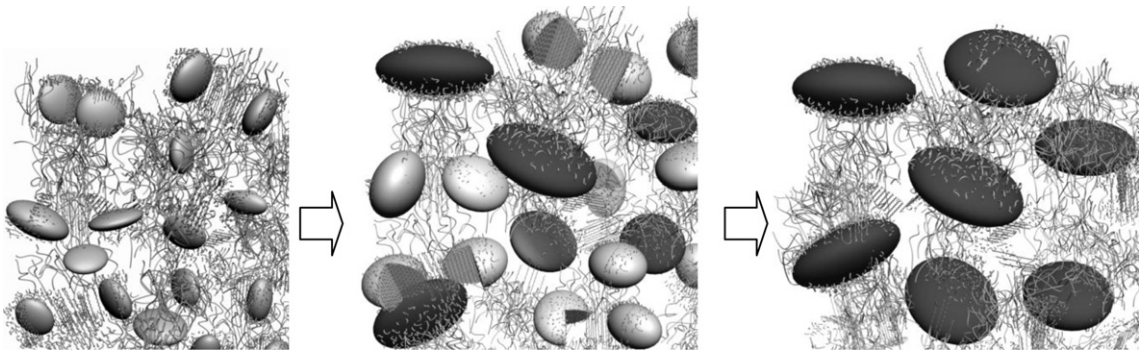

Fig. 6. Cartoons for the as-cast (smaller and denser) β nanograins (left-hand-side) and the β-to-α transition (middle) of PFH, via melting and coalescence of matured β nanograins (along chain axes on the edges of open disks) into larger α nanograins. The structural transition to larger nanograins of better 3D crystalline structure and a larger intergrain spacing (right-hand-side) deteriorates largely the emission features as shown in Fig. 9.

120 °C to $R_g \approx 10$ nm at 160 °C) suppress formation of α crystallite until 190 °C, followed by not only extensive melting but also significant transformation of the β nanograins into α nanocrystals of $R_g \approx 13$ nm in a narrow temperature range of 190–200 °C. Thus transformed α crystallites remained stable in size until melting above 235 °C.

3.2. Cold-crystallization from nematic glass

For the quenched nematic glass, SAXS/WAXS profiles obtained during programmed heating from 30 to 280 °C at 10 °C/min can be interpreted with a previously proposed sequence of nanograin evolution through nucleation, growth, and coalescence before final melting; crystallization into α form took place inside the nanograins in the growth stage starting at ca. 135 °C (Fig. 7). Detailed analysis, following that in the previous studies [19,20], is detailed in SI. Figs. 7 and 8 summarize the structural information obtained from in-situ SAXS/WAXS/DSC for the cold crystallization process of PFH. Below T_1 ($\approx$ 125 °C) is the eventless frozen-in stage. Between T_1 and T_2 ($\approx$ 130 °C) is the nucleation stage, where prolate nuclei of similar size emerge and increase in number. In the growth stage between T_2 and T_3 ($\approx$ 160 °C), nanograins (of fixed concentration n_p and *mean* center-to-center intergrain spacing d) grow significantly, resulting in rapidly increased $X_{c,WAXS}$ (Fig. 7b). Thermal events concerning cold crystallization are essentially completed at the end of this stage as revealed by DSC (Fig. 7d), although WAXS results (Fig. 7c) indicate an on-going development in the long-range positional order (Fig. 7b).

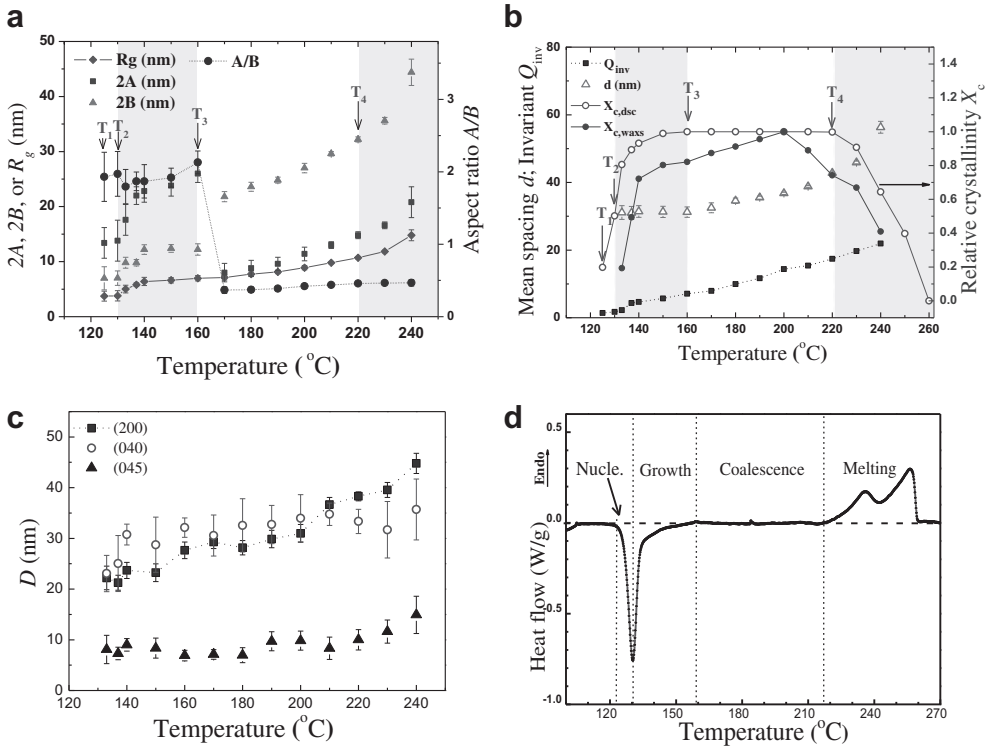

Fig. 7. (a) Changes in semi-major axis 2*A* and semi-minor axis 2*B*, aspect ratio *A*/*B*, and R_g of ellipsoidal nanograins during the programmed heating at 10 °C/min up to 240 °C for melt-quenched PFH. (b) Changes in the fitted mean center-to-center inter-grain spacing *d*, the normalized scattering invariant Q_{inv}, and normalized crystallinities extracted respectively from the corresponding DSC trace ($X_{c,DSC}$) and WAXS profiles ($X_{c,WAXS}$). Highlighted are onset temperatures of nucleation ($T_1 \approx 125$ °C), growth ($T_2 \approx 130$ °C), coalescence ($T_3 \approx 160$ °C), and pre-melting ($T_4 \approx 220$ °C) processes. (c) α crystal dimension *D* calculated from the peak widths of the representative peaks labeled in Fig. S3a using the Scherrer equation. (d) DSC trace obtained at 10 °C/min, showing thermal events of cold-crystallization upon heating of the nematic glass beyond 120 °C and partial melting/reorganization of thus-formed α crystals above 220 °C before final melting above 250 °C.

Author's personal copy

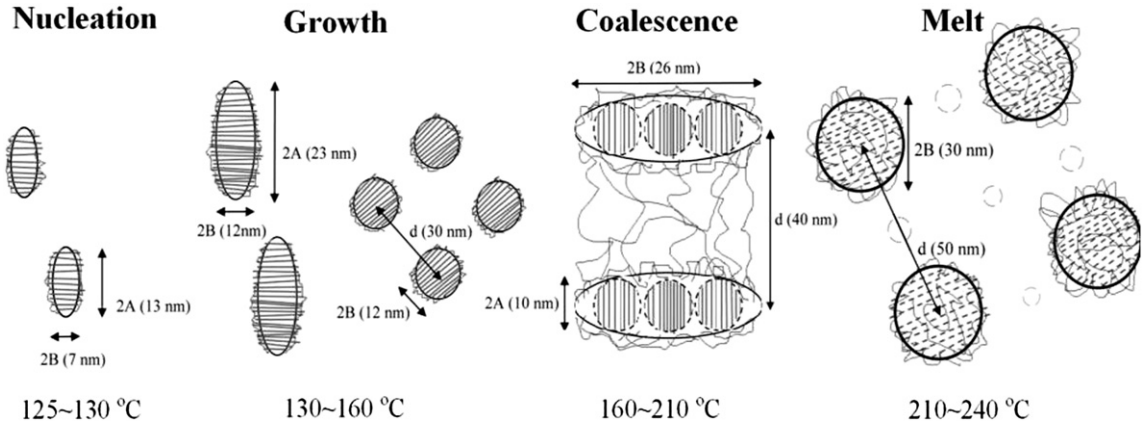

Fig. 8. Cartoons (left to right) illustrating structural evolution of cold-crystallized nanograins from the nucleation stage (sparsely emerged prolate nuclei, side view) to the growth stage (prolate ellipsoids, side and end views transverse to chain axes), the coalescence stage (oblate ellipsoids, side view transverse to chain axes), and the pre-melting/reorganization stage (oblate ellipsoids, top view along chain axes).

The range of T_3–T_4 ($\approx$ 220 °C) is the coalescence stage, where the nanograins grow by coalescence, resulting in a rapid increase in size, especially along the plane of minor oblate axis. This coalescence process does not involve any discernible thermal event as compared to the growth stage (Fig. 7d). On the other hand, the crystallinity $X_{c,WAXS}$ extracted from the WAXS profiles is increasing in this stage with intensified/sharpened ($hk0$) reflections (Fig. 7c). These results indicate improved long-range positional order transverse to the molecular axis that is consistent with the steadily increasing lateral size up to 32 nm ($2B$) at 220 °C. Note that the aspect ratio of nanograins remains approximately fixed at $A/B \approx 0.46$ throughout the coalescence stage, which may be considered characteristic to matured α nanograins (Fig. 7a).

Above T_4 is the pre-melting stage, the nanograin size and interparticle distance increase more strongly than in the preceding stages whereas the crystallinity (either $X_{c,WAXS}$ or $X_{c,DSC}$) decreases (Fig. 7b). Note that although we have used a monodisperse form factor to fit SAXS profiles, the fitted size/shape parameters represent only weighted averages of the actual distribution which is rather narrow in the nucleation stage but not necessarily so afterward. The quickly decreased crystallinity to 40% at 240 °C from 200 °C (Fig. 7b) may therefore be attributed to pre-melting of thinner nanograins, which leaves thicker nanograins the chance of further thickening, growth, and coalescence. In contrast, α crystallites of a relatively uniform size formed from the β-to-α transition exhibit higher thermal stability in this temperature range, resulting in better stabilized relative crystallinity of 70% at 240 °C (cf. Fig. 2b). In the later stages of crystallization, the nanograin dimensions $2A$ and $2B$ (Fig. 7a) obtained from the SAXS results, ca. 20 and 45 nm at 240 °C, are comparable to the crystal dimension D, ca. 15 and 45 nm (Fig. 7c), deduced from corresponding WAXS $(045)_\alpha$ and $(200)_\alpha$ reflections, suggesting that matured α-nanograins are fully crystallized.

3.3. Phase-dependent optical absorption and photoexcited emission

Shown in Fig. 9a and b are optical absorption spectra and the corresponding photoexcited emission spectra of solution-cast PFH films during heating from 30 to 280 °C. In general, much stronger absorption and enhanced emission spectra were observed below 180 °C, associating with the existence of β phase (cf. Fig. 4). Successive decay of these spectra at temperatures above 200 °C reveals increasingly serious deteriorations in absorbance and emission presumably owing to the formation of α crystallites via the β-to-α transition. When heated above 260 °C for a melt of PFH, the absorption and emission features were largely diminished. These results indicate critical influences of the existence of β phase, as demonstrated previously [2–5]. Furthermore, scrutinizing the emission spectra in Fig. 9b, we could quantitatively correlate the strongest emission (peaked at 446 nm) occurred at 140 °C with the observed structural features (WAXS results in Fig. 4), suggesting optimal domain size (7 nm, 20 nm) of the β nanograins along the 2D lattice axes (a, b) for enhanced photoexcited emission in the heat-treated specimens; correspondingly, SAXS data at 140 °C reveal consistent oblate β nanograins of dimensions $2A = 7$ nm and $2B = 20$ nm (cf. Fig. 2a). This relative optimal structure corresponds to ca. five (smectic-like) stacked chains and 22 aligned monomers along the backbone, based on the two lattice parameters ($a = 1.38$ nm, $b = 0.88$ nm) extracted, together with an inter-nanograin spacing of 30 nm as illustrated by the cartoon in Fig. 6. During the β-to-α transition, deteriorated emissions at 180 °C shown in Fig. 9b, however, imply suppression of emission by the perfection of the β nanograin of an increased ordering length to 20 nm along the smectic layering (a) direction. Concomitantly, inter-domain spacing of β nanograins increases from 30 nm at 140 °C to 40 nm at 180 °C (cf. Fig. 2b and Fig. 6), which is likely to hinder hole transport in the PFH film.

Shown in Fig. 9c and d are the corresponding optical absorption and photoexcited emission spectra of PFH films during a similar heating process but in the absence of β nanograins. The temperature dependent emission features observed are, in general, inferior to that observed with existence of β nanograins, implying that formation and growth of α crystallites with temperature (cf. structural evolution of α nanograins elucidated in Fig. 8) are harmful to the photoexcited emissions of the film. On the basis of nanograin structures of β and α phases, these phase-dependent optical absorption and photoexcited emission results reveal delicate effects from size and spatial distribution of β nanograins (of 2D-ordered molecular packing) in tuning electroluminescence behavior of the polyfluorene film. In view of the more monochromatically blue emission of the homologous PFO films solvent-cast for a similar but less structured β mesomorph (which dissipates at a lower temperature around 100 °C [1,7]), we speculate that the much better ordered β mesomorph with stronger intermolecular interactions in the case of PFH may be related to the more broadened emission that is not favored in blue-light device applications.

Author's personal copy

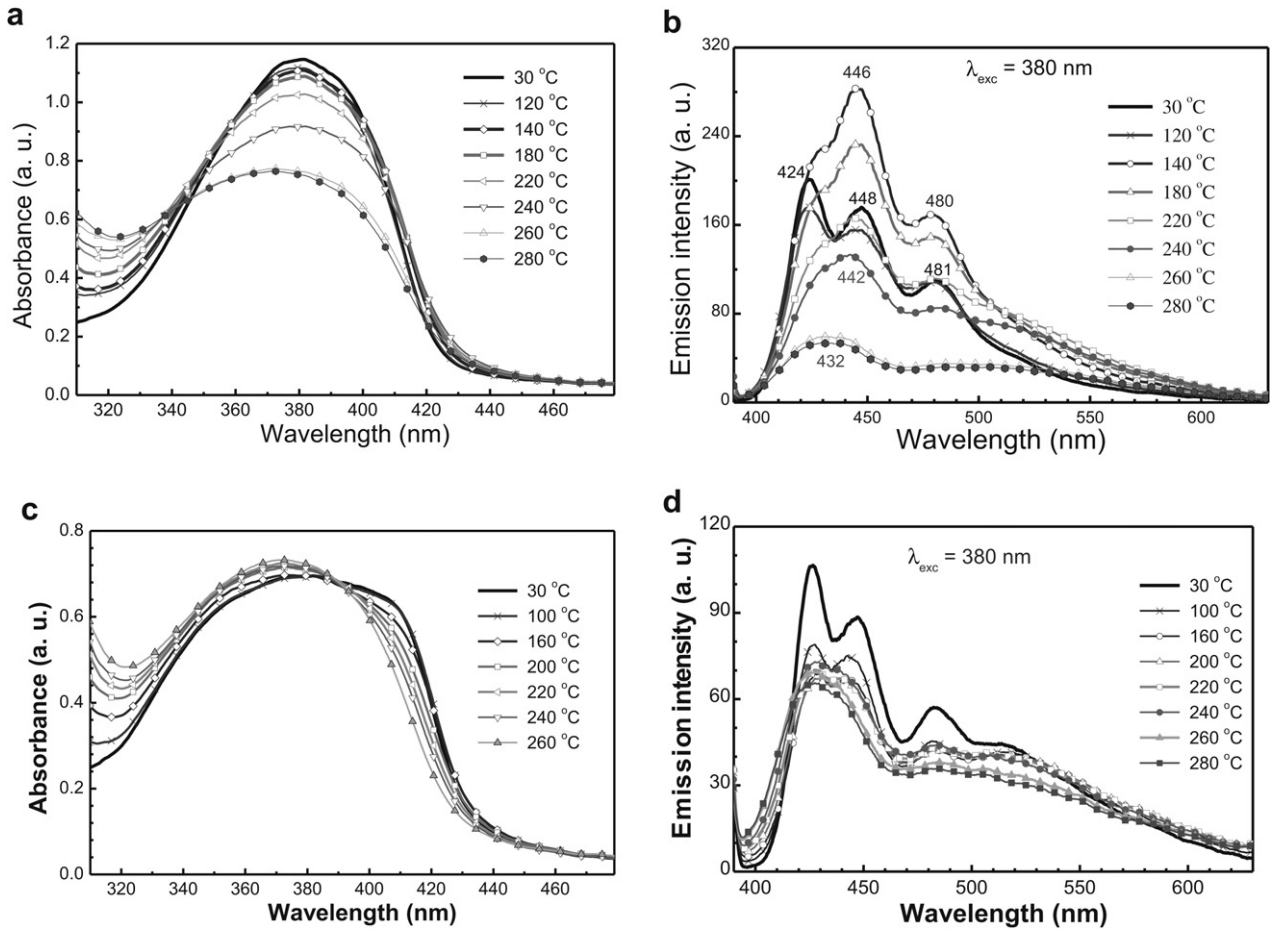

Fig. 9. (a) Optical absorption and (b) photoexcited emission spectra during heating from 30 to 280 °C of solution-cast PFH films containing β phase. Corresponding (c) absorption and (d) emission spectra for the films (quenched from 280 °C, devoid of β phase) reheated with the same heating process.

4. Conclusion

The presented SAXS/WAXS results indicate that the nanograins formed from the nematic melt bear α crystalline features at ~135 °C. In general, the cold crystallization process of PFH from nematic glass follows the sequence of nucleation, growth/crystallization, and coalescence (upon programmed heating) or reorganization of nanograins, as that similarly observed for PFO, sPS, and PTT. In contrast, the mesomorphic β phase of the solution-cast PFH carries readily oblate-like nanograins of 2D-ordered molecular packing. Development of the mesomorphic β phase into α crystals is described by nanograin evolution with characteristically different stages of growth/coalescence of β nanograins and fast transition from β to α phases. Growth/coalescence of β nanograins, effectively suppresses the formation of α nanograins until ca. 190 °C, at which the efficient transformation from β phase to the thermodynamically favored α phase is activated by partial melting and reorganization of β nanograins into α crystallites of higher thermal stability. Within the present heat-treatment approach, optimal photoexcited emission of PFH corresponds to mesomorphic β nanograins ca. 7 and 20 nm along the 2D lattice axes *a* and *b*, respectively, with intergrain spacing of ca. 30 nm; overgrown β phase is harmful for emission properties, whereas development of α phase is fatal. In general, the sensitive influences of the mesomorphic β phase development on the emission properties suggest a nanostructural origin for the thermal instability of the PFH emission properties.

Acknowledgments

AcknowledgmentsThis work was financially supported by the National Science Council (contract numbers NSC 98 2221 E 007 009 MY3 and NSC 99 2112 M 213 002 MY3). Helps from Ms. K.-F. Liao and Mr. W.-B. Su in SAXS/WAXS measurements are gratefully acknowledged.

Appendix A. Supplementary data

Supplementary data related to this article can be found, in the online version, at http://dx.doi.org/10.1016/j.polymer.2012.07.024.

References

[1] Chen SH, Su AC, Su CH, Chen SA. J Phys Chem B 2005;109:10067–72.
[2] Li HH, Liu CY, Chang CH, Chen SA. Adv Mater 2007;19:2574–9.
[3] Cadby AJ, Lane PA, Mellor H, Martin SJ, Grell M, Giebeler C, et al. Phys Rev B 2000;62:15604–9.
[4] Ariu M, Sims M, Rahn MD, Hill J, Fox AM, Lidzey DG, et al. Phys Rev B 2003;67:195333–43.
[5] Kilina S, Batista ER, Yang P, Tretiak S, Saxena A, Martin RL, et al. ACS Nano 2008;2:1381–8.
[6] Chen CY, Chang CS, Huang SW, Chen JH, Chen HL, Su CI, et al. Macromolecules 2010;43:4346–54.
[7] Chen SH, Su AC, Su CH, Chen SA. Macromolecules 2005;38:379–85.
[8] Chen SH, Su AC, Su CH, Chen SA. Macromolecules 2006;39:9143–9.
[9] Kaji K, Nishida K, Kanaya T, Matsuba G, Konishi T, Imai M. Adv Polym Sci 2005;191:187–240. and references cited therein.

Author's personal copy

[10] Heeley EL, Poh CK, Li W, Maidens A, Bras W, Dolbnya IP, et al. Faraday Discuss 2003;122:343–61.
[11] Wang ZG, Hsiao BS, Sirota EB, Srinivas S. Polymer 2000;41:8825–32.
[12] Fougnies C, Damman P, Villers D, Dosiere M, Koch MHJ. Macromolecules 1997;30:1385–91.
[13] Mano JF, Wang Y, Viana JC, Denchev Z, Oliveira MJ. Macromol Mater Eng 2004; 289:910–5.
[14] Terrill NJ, Fairclough JPA, Towns-Andrews E, Komanschek BU, Young RJ, Ryan AJ. Polymer 1998;39:2381–5.
[15] Imai M, Kaji K, Kanaya T. Phys Rev Lett 1993;71:4162–5.
[16] Konishi T, Nishida K, Kanaya T. Macromolecules 2006;39:8035–9040.
[17] Strobl G. Eur Phys J E 2000;3:165–83.
[18] Ryan AJ, Fairclough JPA, Terrill NJ, Olmsted PD, Poon WCK. Faraday Discuss 1999;112:13–29.
[19] Su CH, Jeng U, Chen SH, Lin SJ, Ou YT, Chuang WT, et al. Macromolecules 2008; 41:7630–6.
[20] Su CH, Jeng U, Chen SH, Lin SJ, Wu WR, Chuang WT, et al. Macromolecules 2009;42:6656–64.
[21] Chuang WT, Su WB, Jeng U, Hong PD, Su CJ, Su CH, et al. Macromolecules 2011;44:1140–8.
[22] Chen SH, Su AC, Su CH, Chen SA. J Phys Chem B 2006;110:4007–13.
[23] Rahman MH, Chen CY, Liao SC, Chen HL, Tsao CS, Chen JH, et al. Macromolecules 2007;40:6572–8.
[24] Knaapila M, Alma'sy L, Garamus VM, Ramos ML, Justino LLG, Galbrecht F, et al. Polymer 2008;49:2033–8.
[25] Chen SH, Chou HL, Su AC, Chen SA. Macromolecules 2004;37:6833–8.
[26] Brinkmann M. Macromolecules 2007;40:7532–41.
[27] Lan YK, Su AC. Macromolecules 2010;43:7908–12.
[28] Heck B, Perez E, Strobl G. Macromolecules 2010;43:4172–83.
[29] Jeng U, Su CH, Su CJ, Liao KF, Chuang WT, Lai YH, et al. J Appl Cryst 2010;43:110–21.
[30] Chen SH, Lin TL. In: Sköld K, Price DL, editors. Methods of experimental physics–Neutron scattering in condensed matter research, vol. 23B. New York: Academic; 1987 [ch. 16].
[31] Feigin LA, Svergun DI. Structure analysis by small-angle X-ray and neutron scattering. New York: Plenum; 1987. 69.
[32] Smilgies D-M. J Appl Cryst 2009;42:1030–4.